2015 IEEE/RSJ International Conference on Intelligent Robots and Systems (IROS)
Congress Center Hamburg
Sept 28 - Oct 2, 2015. Hamburg, Germany

Stabilizing the Relative Position of Millirobots inside an MRI Scanner Considering Magnetic Interaction Forces

Alina Eqtami and Pierre E. Dupont

Abstract— **The concept of navigating groups of magnetically propelled particles through the fluid-filled passageways of the body provides the potential to perform highly localized diagnostic and therapeutic procedures. The use of MRI scanners to both navigate and propel millimeter-scale robots has received recent attention. MRI-based motion planning and control laws have been proposed that can achieve independent position control of multiple robots despite the system being underactuated, i.e., the same magnetic gradients are experienced by all the robots. To date, however, these analyses have neglected the magnetic interaction forces and torques between these robots. Thus, the question of whether or not the relatively weak gradients can stabilize the particles as they approach each other has remained open. This paper investigates this question by analyzing interaction forces and torques experienced inside an MRI scanner. It is shown that interaction torques can be neglected in the presence of the strong central field of the scanner. Using the reduced force-based model, a lower bound on separation distance is derived and it is shown that this bound could be achieved if the system was fully actuated. Considering underactuation, simulation demonstrates that Model Predictive Control can stabilize pairs of robots at separation distances 2.5-3 times the lower bound on separation distance.**

I. Introduction

Miniature tetherless robots can facilitate access to locations inside the human body that would otherwise be difficult or even impossible to reach. For example, these robots can be injected into the circulatory system or into the spinal canal and navigated to various organs including the brain. Groups of such robots can be employed to deliver drugs and cells or to set up sensor networks to monitor physiologic conditions or to detect specific circulating cells.

Prior work has considered magnetic actuation at the micron [1], [2], [3], nano [4] and millimeter scale [5]. Initial efforts focused on the control of single magnetic robots [6], [7], [8], whereas recent research has addressed the control of groups of robots [9], [10], [5].

Magnetic control of groups of robots is challenging since such systems are underactuated, i.e., all the robots are exposed to the same magnetic field. Independent control relies on inducing a heterogeneous dynamic response to the magnetic field by exploiting differences in, e.g., drag forces as well as the volume and distribution of magnetic material [11], [5].

This work was supported by the National Science Foundation under grant IIS-1208509 and by the Wyss Institute for Biologically Inspired Engineering.

A. Eqtami and P.E. Dupont are with with Cardiac Surgery, Boston Children's Hospital, Harvard Medical School, 02115 Boston, Massachusetts. {firstname.lastname@childrens.harvard.edu}

Most of these systems are actuated using custom-made coils that fit on the bench top. Creating coils large enough to enclose the human body is feasible albeit expensive [12]. Alternatively, MRI scanners are already available at most hospitals and also provide imaging capabilities. Consequently, MRI-based robot navigation has been considered by several researchers [13], [14].

Actuation using an MRI scanner, while similar in some respects to tabletop coil systems, has some important differences. First, the strong static central field of the scanner magnetizes any ferromagnetic material placed inside the scanner bore and causes it to align with the central field. While this avoids the need to construct robots using permanent magnets, the static nature of the field precludes the use of magnetic torque in robot control. Any angular perturbation of the magnetized robot from alignment with the central field produces an extremely large restoring torque. As explained later in the paper, this effect causes magnetized robots to repel each other when placed side by side in the bore, but attract each other when placed collinearly with the central axis.

Without the capability to control torque, robot motion control is based on using magnetic gradients to generate forces. Similar to coil-based systems, MRI-based multi-robot control is underactuated since all robots experience the same gradients in the three coordinate directions.

To address multi-robot position control, [5] introduced a motion planning algorithm that exploited differences in millirobot response to gradient pulses. The algorithm generated sequences of pulses of varying sign and width that could drive buoyant millirobots to desired positions on the planar surface of a fluid from arbitrary initial conditions. As a motion planner, this approach is open loop and it also assumed that the robots were far enough apart that magnetic interaction effects could be neglected.

A closed-loop framework for multi-robot position control was introduced in [10] that incorporated consideration of robustness as well as a novel framework for optimal switching between actuation and tracking while preserving stability. Similar to [5], however, this work assumed that robot magnetic interaction is negligible.

The contribution of this paper is to answer the question of how close a pair of swimming millimeter-scale robots can stably approach each other without colliding under closed-loop control in an MRI scanner. The remainder of the paper is organized as follows. Section II presents the dynamic equations of the system of two robots and discusses the forces and torques acting on the two robots. In Section III the

978-1-4799-9994-1/15/$31.00 ©2015 IEEE

control formulation is defined and in Section IV validation examples, illustrating stabilized trajectories for the various regions, are presented. Finally, conclusions are drawn in Section V.

II. Dynamic Equations

To arrive at the dynamic equations, some preliminary concepts are first defined. Consider a magnetic dipole in a Euclidean workspace $\mathcal{W} \subseteq \mathbb{R}^3$. The dipole moment $\vec{\mathbf{m}}$ of the physical dipole, using the magnetic pole model, is formed by two opposite magnetic poles separated by a small distance vector $\vec{\mathbf{d}}$, where $\vec{\mathbf{d}}$ is the vector from the South to the North pole. Hereafter, the robots are going to be modeled as point magnetic dipoles. The magnetization of a material $\vec{\mathbf{M}}_s$ represents how strongly a region of material is magnetized. Hence, the dipole moment can be defined as $\vec{\mathbf{m}} = \vec{\mathbf{M}}_s V$, where V is the volume of the dipole. Assume now, that $\mathcal{O}$-**xyz** is a base frame and that it is centered at the isocenter of the bore of the MRI scanner, with the **z**-axis directed along the axis of the bore and that $\mathcal{C}$-**xyz** is the origin of an orthogonal reference frame placed at the point dipole. The magnetic field of the magnetic point dipole, defined by a dipole moment $\vec{\mathbf{m}} \in \mathbb{R}^3$ in a workspace $\mathcal{W} \subset \mathbb{R}^3$ is given as:

$$\vec{\mathbf{B}}_d(\vec{\mathbf{m}}, \vec{\mathbf{r}}) = \frac{\mu_0}{4\pi r^3}(3(\vec{\mathbf{m}} \cdot \hat{r})\hat{r} - \vec{\mathbf{m}}) + \frac{2\mu_0}{3}\vec{\mathbf{m}}\delta^3(r) \quad (1)$$

where $\vec{\mathbf{r}} \triangleq [r_x, r_y, r_z]^\top = r\hat{r}$, denotes a vector from $\mathcal{C}(0,0,0)$ to a point p and $r \triangleq \sqrt{r_x^2 + r_y^2 + r_z^2}$, $\hat{r}$ denote its length and unit vector, respectively. The constant μ_0 is called vacuum permeability and is equal to $4\pi 10^{-7}$ Vs/Am. Moreover, the function $\delta^3(\cdot)$ is a 3-dimensional Dirac Delta function which vanishes everywhere except for one particular point of its argument, $\vec{\mathbf{r}} = [0,0,0]^\top$.

For comparison with prior work, it is assumed that the robots move in the horizontal **xz** plane with buoyancy and gravitational forces in balance. The motion of the two robots R_1 and R_2 depends on the following forces: $\vec{\mathbf{F}}_m$ i.e., the magnetic forces induced by the gradient coils of the MRI, $\vec{\mathbf{F}}_d$ i.e., the fluid drag forces opposing robot motion and $\vec{\mathbf{F}}_i$, i.e., the dipole interaction forces neglected in prior work [10], [5].

The force equations are given by:

$$M_1\vec{\mathbf{a}}_1 = \vec{\mathbf{F}}_{d_1} + \vec{\mathbf{F}}_{m_1} + \vec{\mathbf{F}}_{i_{12}} \quad (2a)$$

$$M_2\vec{\mathbf{a}}_2 = \vec{\mathbf{F}}_{d_2} + \vec{\mathbf{F}}_{m_2} + \vec{\mathbf{F}}_{i_{21}} \quad (2b)$$

where M_1, M_2 and $\vec{\mathbf{a}}_1$, $\vec{\mathbf{a}}_2$ are the mass and acceleration terms for each robot R_1 and R_2, respectively.

The robots also experience torques due to the magnetic fields of the MRI and their own interacting fields. Consider that the robot's magnetic moment $\vec{\mathbf{m}}$ forms an angle ϕ with respect to the **z**-axis, as it shown in Fig.1. The following dynamic equations describe the resulting motion:

$$J_1\ddot{\phi}_1 = \vec{\mathbf{T}}_{d_1} + \vec{\mathbf{T}}_{m_1} + \vec{\mathbf{T}}_{i_{12}} \quad (3a)$$

$$J_2\ddot{\phi}_2 = \vec{\mathbf{T}}_{d_2} + \vec{\mathbf{T}}_{m_2} + \vec{\mathbf{T}}_{i_{21}} \quad (3b)$$

Here J_1, J_2 are the moments of inertia of the two robots and ϕ_1, ϕ_2 are the angles that correspond to the magnetic moments $\vec{\mathbf{m}}_1$ and $\vec{\mathbf{m}}_2$ of robots R_1 and R_2 with respect to the **z**-axis, respectively. The terms $\vec{\mathbf{T}}_{d_1}$ and $\vec{\mathbf{T}}_{d_2}$ represent fluid drag torques. Moreover, $\vec{\mathbf{T}}_{m_1}$, $\vec{\mathbf{T}}_{m_2}$ are the torques acting on the robots due to the presence of the very strong and uniform magnetic field $\vec{\mathbf{B}}_0$ of the MRI scanner, which is directed along the **z**-axis. Each of the robots, however, is experiencing a torque acting on it due to the other robot's magnetic field, namely, $\vec{\mathbf{T}}_{i_{12}}$ and $\vec{\mathbf{T}}_{i_{21}}$. Expressions for the forces (2a)-(2b) and the torques (3a)-(3b) are derived in the following subsections.

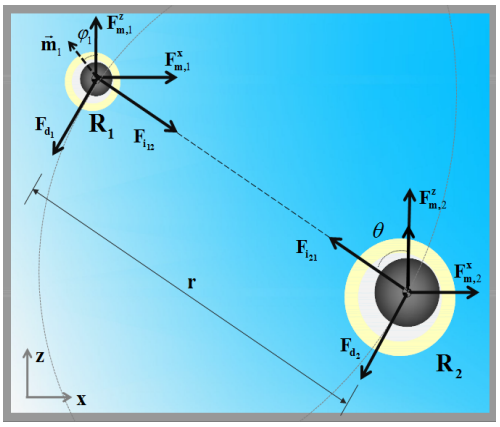

Fig. 1. Plan view of two encapsulated ferromagnetic robots R_1 and R_2, immersed into a water tank.

A. Contribution of Magnetic Torques

The torques that are acting on the robots due to the MRI's magnetic field $\vec{\mathbf{B}}_0$ can be described as follows:

$$\vec{\mathbf{T}}_m = V\vec{\mathbf{M}}_s \times \vec{\mathbf{B}}_0 \quad (4)$$

where V is the magnetic volume of the material and $\vec{\mathbf{M}}_s$, is the saturated magnetization per unit volume of the material. Moreover, the torque generated on robot R_1 by robot R_2 is given by, [15]:

$$\vec{\mathbf{T}}_{i_{12}} = \frac{\mu_0}{4\pi r^5}\big(3\vec{\mathbf{m}}_2 \times (\vec{\mathbf{m}}_1 \cdot \vec{\mathbf{r}}) \cdot \vec{\mathbf{r}} - r^2(\vec{\mathbf{m}}_2 \times \vec{\mathbf{m}}_1)\big) \quad (5)$$

Since the torques generated by the central field are so large, it may be possible for purposes of computing robot position to assume that the robots remain aligned with the central field. To investigate this possibility, it is assumed here that the center of each robot is constrained in the plane, but that each is free to rotate about its center. Under this assumption, (4)-(5) can be used to compute an analytical expression for the equilibrium angles $\phi_1^\star$ and $\phi_2^\star$ of (3a)-(3b), for the two robots R_1 and R_2, respectively.

The tangent of the angle $\phi_1^\star$ is given by:

$$\tan\phi_1^\star = \frac{3||\vec{\mathbf{m}}_1||\mu_0 \sin\theta\cos\theta}{4\pi r^3||\vec{\mathbf{B}}_0|| + \mu_0||\vec{\mathbf{m}}_1|| + 3||\vec{\mathbf{m}}_1||\mu_0\sin^2\theta} \quad (6)$$

where $\vec{\mathbf{r}}$ is the vector that connects the centers of the robots and forms an angle θ with respect to the **z**-axis, as depicted

in Fig.1. Using data from Table I of the validation section, we can derive the following equilibrium angles: Considering that $||\vec{\mathbf{B}}_0|| = 3$ Tesla, a (minimum) separation distance of $||\vec{\mathbf{r}}|| = 3.2$ mm, and for $\theta \in [0, 2\pi)$, it can be found that for a robot of diameter $d_1 = 1.5$mm, the equilibrium angle is $\phi_1^\star \in \{-0.2°, \ldots, 0.2°\}$.

Since the effect of these small angles on the direction of the magnetic gradient and interaction forces is negligible, robot rotational dynamics will not be considered in the remainder of the paper and, in the force analysis, it will be assumed that the robot dipoles remain aligned with the central field axis, **z**.

B. Gradient and Damping Forces

The MRI scanner is comprised of electromagnetic coils: the main coil that produces the $\vec{\mathbf{B}}_0$ field and the gradient coils that generate a magnetic field $\vec{\mathbf{B}}_g$. The magnitude of the magnetic field $\vec{\mathbf{B}}_g$ along the **z**-direction can be linearly modified along any direction in **xyz**-coordinates by the gradients coils. The forces $\vec{\mathbf{F}}_m$ that are applied to a magnetic robot by the magnetic fields $\vec{\mathbf{B}} = \vec{\mathbf{B}}_0 + \vec{\mathbf{B}}_g$, are given by:

$$\vec{\mathbf{F}}_m = V(\vec{\mathbf{M}}_s \nabla)\vec{\mathbf{B}} \tag{7}$$

In particular, the force $\vec{\mathbf{F}}_m$ acting on each robot, with respect to the base frame $\mathcal{O}$-**xyz**, can be analyzed as follows:

$$[F_m^x,\, F_m^y,\, F_m^z]^\top = V M_{sz}[\frac{\partial B_{gx}}{\partial z},\, \frac{\partial B_{gy}}{\partial z},\, \frac{\partial B_{gz}}{\partial z}]^T \tag{8}$$

where it was assumed that $M_{sx}, M_{sy} \ll M_{sz}$. In [16], it was shown that the gradients in (8) are linearly independent and thus provide three degrees of freedom of motion to every ferromagnetic body that is inside the MRI bore.

Since the magnetic material is contained inside hollow capsules, the robots experience buoyancy forces that counteract the gravitational forces as well as the small component of the interaction force that is acting on each robot along the **y**-axis (due to the dimension difference of the robots). Furthermore, the motion of the robots is opposed also by drag forces $\vec{\mathbf{F}}_d$, due to the presence of the fluid. The drag force for each robot is given by:

$$\vec{\mathbf{F}}_d = \frac{1}{2}\eta C_d A v^2 \tag{9}$$

where η is the density of the water, C_d is a drag coefficient parameter, A is the frontal area of the robot and finally, v is the robot's velocity. More information for the use of this drag force model can be found in [5].

C. Dipole-dipole Interaction Forces

The force acting on the robot R_2 due to the presence of the robot R_1 is given by, [17]:

$$\begin{aligned}\vec{\mathbf{F}}_{i_{21}} = \frac{3\mu_0}{4\pi r^5}\big(&\vec{\mathbf{r}}(\vec{\mathbf{m}}_1 \cdot \vec{\mathbf{m}}_2) + \vec{\mathbf{m}}_1(\vec{\mathbf{r}} \cdot \vec{\mathbf{m}}_2) \\ &+ \vec{\mathbf{m}}_2(\vec{\mathbf{r}} \cdot \vec{\mathbf{m}}_1) - 5\frac{\vec{\mathbf{r}}}{r^2}(\vec{\mathbf{r}} \cdot \vec{\mathbf{m}}_1)(\vec{\mathbf{r}} \cdot \vec{\mathbf{m}}_2)\big)\end{aligned} \tag{10}$$

It can easily be shown that the force $\vec{\mathbf{F}}_{i_{12}}$ exerted by R_2 on R_1 is equal and opposite to $\vec{\mathbf{F}}_{i_{21}}$.

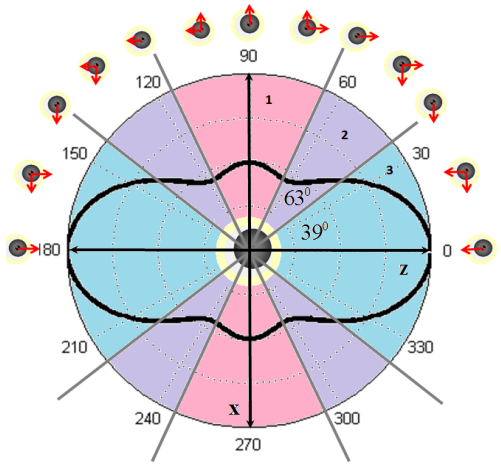

Fig. 2. Direction of magnetic interaction forces with respect to scanner axis. Region 1 (pink) is repulsive. Region 3 (blue) is attractive. Region 2 (purple) is unstable. Red arrows show the force components acting on a robot due to the presence of the centrally located robot. The black solid curve depicts the magnitude of the force for a specific relative distance between the two robots.

Under the assumption that the robot dipoles remain aligned with the central field of the scanner, (10) can be shown to produce robot interaction forces that depend on the relative angle of the robots with respect to the central field axis as shown in Fig. 2. In this figure, one robot is depicted at the center and the second robot is shown around the periphery of a circle marked with the angle relative to the central field (**z**-axis). As shown by the red arrows, the robots are attracted to each other when roughly collinear with the **z**-axis. On the other hand, when placed roughly along the **x**-axis, they repel each.

To investigate this effect in more detail, the force components $\vec{\mathbf{F}}_{i_{21}} = [F_{i_{21}}^x, F_{i_{21}}^z]^\top$ can be written as

$$F_{i_{21}}^x = \frac{3\mu_0 \vec{\mathbf{m}}_1 \cdot \vec{\mathbf{m}}_2}{4\pi r^4}(sin\theta - 5sin\theta cos^2\theta) \tag{11a}$$

$$F_{i_{21}}^z = \frac{3\mu_0 \vec{\mathbf{m}}_1 \cdot \vec{\mathbf{m}}_2}{4\pi r^4}(3cos\theta - 5cos^3\theta) \tag{11b}$$

where θ is the angle formed by the distance vector $\vec{\mathbf{r}}$ and **z**-axis.

The zeros of the components in the interval $\theta \in [0, 2\pi)$ are given below and labeled with radial lines in Fig. 2.

$$F_i^x(\theta) = 0,\ \forall\, \theta = \{0°, 63°, 117°, 180°, 243°, 297°\} \tag{12a}$$

$$F_i^z(\theta) = 0,\ \forall \theta = \{39°, 90°, 141°, 219°, 270°, 321°\} \tag{12b}$$

These force component zeroes divide the angular space into three regions, which are color-coded and numerically labeled in the figure. Region 1 corresponds to the repulsive zone while region 3 is attractive. While not shown here, robot pairs with zero initial velocity starting in these regions remain in their respective region moving either farther apart or colliding. In contrast, robots starting in Region 2 tend to move into Region 1. The force magnitude for a specific $\vec{\mathbf{r}}$ is given by the black curve in Fig. 2. It is clear from the figure that no equilibrium points, stable or unstable, exist for the uncontrolled system.

D. Lower Bound on Minimum Separation Distance

We are interested in whether or not, through the introduction of a controller, the two robots can be stabilized with respect to each other. There are two significant constraints, however, in implementing closed-loop control. These are that the gradient forces are bounded and that the gradient forces are the same for both robots. This section derives a lower bound considering only gradient force saturation while ignoring underactuation.

To do so, it is assumed that one robot is fixed in position while the other is held at a desired equilibrium position by balancing interaction forces and gradient forces. Minimum separation distance corresponds to saturation of at least one gradient coil. Taking into consideration (7) and (11a)-(11b), the minimum separation distance can be found as follows:

$$r_{\min}(\theta) = \max\{r_{ix}(\theta), r_{iz}(\theta)\} \tag{13}$$

where $r_{ix}(\theta)$ and $r_{iz}(\theta)$ are the radii corresponding to saturated gradient forces in the x and z directions, respectively, for robot i as defined below.

$$r_{ix}(\theta) \triangleq \Big(\frac{3\mu_0 \vec{\mathbf{m}}_1 \cdot \vec{\mathbf{m}}_2 (sin\theta - 5sin\theta cos^2\theta)}{4\pi V_i M_{sz} \frac{\partial B_{gx}}{\partial z}|_{\max}}\Big)^{\frac{1}{4}}$$
$$r_{iz}(\theta) \triangleq \Big(\frac{3\mu_0 \vec{\mathbf{m}}_1 \cdot \vec{\mathbf{m}}_2 (3cos\theta - 5cos^3\theta)}{4\pi V_i M_{sz} \frac{\partial B_{gz}}{\partial z}|_{\max}}\Big)^{\frac{1}{4}}$$

Since the maximum gradient force depends on the magnetic volume of the individual robot, the equilibrium distance for the smaller robot is smaller than that of the larger robot. This minimum distance of approach is a function of relative angle, θ, and is plotted as the black curve in Fig. 3 using the parameter values of Table I.

TABLE I
ROBOT AND MRI PARAMETERS

Parameters	Value
Diameter of robot R_1 $[mm]$	1.5
Diameter of robot R_2 $[mm]$	3.0
Density of ferrous spheres $[Kg/m^3]$	7850
M_{sz}−Magnetization of ferrous spheres $[Am^{-1}]$	$1.36 \cdot 10^6$
Dynamic viscosity of the fluid $[Pas]$	$1.00 \cdot 10^{-3}$
η-Density of the fluid $[Kg/m^3]$	$1.00 \cdot 10^3$
ν_i-Gradient amplitude $[T/m]$	± 0.04

Given this lower bound on minimum separation distance, two questions arise that are addressed in the remainder of the paper. First, under the assumption that the gradient forces can be applied independently to each robot, can a controller be found that could stabilize all points in an open set outside of (13)? Second, considering that the same gradient field is actually applied to both robots, how closely can this bound be achieved? Since the system is nonlinear, both questions must be answered by assuming a specific controller structure. In the following sections, these questions are addressed using nonlinear model predictive control.

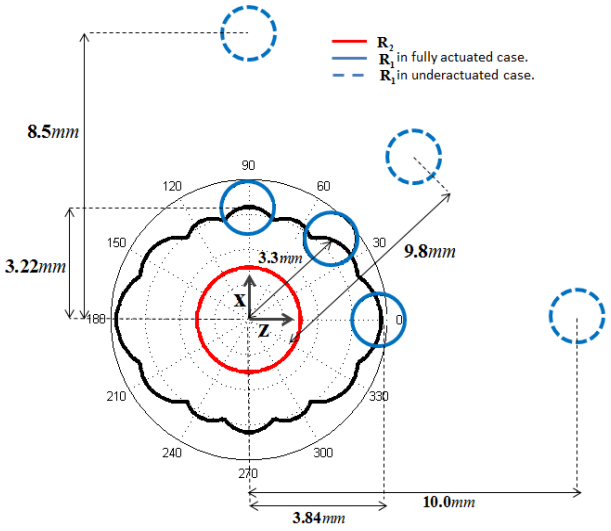

Fig. 3. Minimum stabilizable distance between robot 2 (in red) and robot 1 (in blue). Lower bound is solid black curve. Distances achieved using nonlinear model predictive control (derived in following sections) assuming full actuation and underactuation, respectively, shown in solid blue and dashed blue.

III. CONTROLLER FORMULATION

The state-space model of the two robots in motion along the **xz**-axes can be obtained as follows:

$$\begin{aligned}
\ddot{x}_1 &= -b_1 \dot{x}_1^2 sign(x_1) + g_1 \nu_1 + \mathbf{F}^x_{i_{12}} \\
\ddot{z}_1 &= -b_1 \dot{z}_1^2 sign(z_1) + g_1 \nu_2 + \mathbf{F}^z_{i_{12}} \\
\ddot{x}_2 &= -b_2 \dot{x}_2^2 sign(x_2) + g_2 \nu_1 + \mathbf{F}^x_{i_{21}} \\
\ddot{z}_2 &= -b_2 \dot{z}_2^2 sign(z_2) + g_2 \nu_2 + \mathbf{F}^z_{i_{21}}
\end{aligned} \tag{14}$$

where $g_j \triangleq \frac{V_j M_{sz}}{M_j}$ and $b_j \triangleq \frac{\eta C_{d_j} A_j}{2M_j}$ with $j = 1, 2$. Equations (14) can be written in stack vector form as follows:

$$\dot{\mathbf{x}} = \underbrace{f(\mathbf{x}) + h(\mathbf{x})}_{F(\mathbf{x})} + G\mathbf{u} \tag{15}$$

where we have assumed the following:
$\mathbf{x} \triangleq \begin{bmatrix} x_1 & \dot{x}_1 & z_1 & \dot{z}_1 & x_2 & \dot{x}_2 & z_2 & \dot{z}_2 \end{bmatrix}^\top$ and $\mathbf{u} \triangleq \begin{bmatrix} \nu_1 & \nu_2 \end{bmatrix}^\top \triangleq \begin{bmatrix} \frac{\partial B_{gx}}{\partial z} & \frac{\partial B_{gz}}{\partial z} \end{bmatrix}^\top$, with (x_1, z_1) and (x_2, z_2) to be the positions (x, z) in the $\mathcal{O}$-**xyz**-coordinate system, of the robots R_1 and R_2, respectively and $(\dot{x}_1, \dot{z}_1)$, $(\dot{x}_2, \dot{z}_2)$ to be the corresponding velocity terms. Notice here, that in (15) the term $f(\mathbf{x})$ is related to the drag forces while the term $h(\mathbf{x})$ is related to the interaction forces.

The goal is to drive the two robots from an initial position $\mathbf{x}_{init}$ to a desired final position $\mathbf{x}_f$, without collision. The system (15) is a continuous-time nonlinear control-affine under-actuated system, subject to input and state constraints. The input constraints are imposed by the use of a clinical MRI scanner which has limited range of magnetic gradients that can be applied, i.e. input saturation constraints, and the goal of controlling particles inside the human body will provide restrictions in the states, thus convex state constraints must also be fulfilled.

Nonlinear Model Predictive Control (NMPC) has been shown to be an effective technique for such constrained control problems [18], [19]. This approach relies on iterative, finite horizon optimization which is solved at discrete-time instants k_i, with $k_i \in \mathbb{R}_+$ and $i \to \infty$. At each arbitrary calculation instant k_i, the current state of the system $\mathbf{x}(k_i)$ is measured (or estimated) and a control law is computed. This control law is based on a constrained optimization of a suitable selected cost function over a time interval $[k_i, k_i + T)$, where T is the prediction horizon. The process is repeated when the new state $\mathbf{x}(k_{i+1})$ is available. The optimal control problem of the NMPC is formulated as:

$$\min_{\mathbf{u}(\cdot)} \int_{k_i}^{k_i+T} \big(L_1(\mathbf{x}(\tau)) + L_2(\mathbf{u}(\tau))\big)\, \mathrm{d}\,\tau + V(\mathbf{x}(k_i+T)) \tag{16a}$$

subject to:

$$\dot{\mathbf{x}}(t) = F(\mathbf{x}(t)) + G\mathbf{u}(t) \tag{16b}$$

$$\mathbf{u}(t) \in \mathbb{U}, \quad \mathbf{x}(t) \in \mathbb{X}, \quad t \in [k_i, k_i + T] \tag{16c}$$

$$\mathbf{x}(k_i + T_p) \in \mathbb{X}_f \tag{16d}$$

The sets $\mathbb{X} \in \mathbb{R}^8$ and $\mathbb{U} \in \mathbb{R}^2$ are assumed to be compact. Moreover, the objective functional (16a) consists of a sum of running costs; $L_1(\mathbf{x})$ and $L_2(\mathbf{u})$ represent the whole energy of the system and the control performance, respectively. In particular, $L_1(\mathbf{x})$ and $L_2(\mathbf{u})$ can be of standard quadratic form, i.e., $L_1(\cdot)+L_2(\cdot) = \frac{1}{2}(\mathbf{x}-\mathbf{x}_f)^\top Q(\mathbf{x}-\mathbf{x}_f)+\frac{1}{2}\mathbf{u}^\top R\mathbf{u}$. Furthermore, the terminal inequality constraint (16d) forces the states at the end of the prediction horizon to be in some set $\mathbb{X}_f$ containing the desired state. Finally, the terminal cost $V(\cdot)$ is such that specifies the states at the end of the prediction horizon and it can be also a quadratic function: $V(\cdot) = \frac{1}{2}(\mathbf{x} - \mathbf{x}_f)^\top P(\mathbf{x} - \mathbf{x}_f)$.

Remark 1: The stability and the robustness of an MPC scheme for the control of two robots inside the MRI without considering interaction forces, i.e., having $h(\mathbf{x}) \equiv 0$ in particular, has been presented in [10]. The stability analysis of MPC formulated in (16a)-(16d) is a direct generalization of what is reported in [10] and will not be extensively discussed here. In [10] has been derived that a system without considering interaction forces can be stabilized in the desired position. The additive term $h(\mathbf{x})$ that is being considered in this paper can be seen as a non-vanishing perturbation affecting a nominal system without interaction. As discussed in [20], the state trajectory of stable systems that are affected by non-vanishing, although bounded, perturbations can be proven to converge to the vicinity of the desired position. This will be depicted in the next section with the validation examples.

Remark 2: The MRI scanner provides the means to control and also to track the two robots. The localization of the robots at each sampling instant can be obtained from a tracking sequence of the MRI which is interleaved with an actuation sequence, [10]. Moreover, [10] also provides an efficient way to choose the computation times k_i, under the restrictions of the use of a clinical MRI set-up.

IV. Minimum Separation Distance Under Closed-loop NMP Control

To address the questions of how closely the lower bound on minimum separation distance can be approached under closed-loop control, two scenarios are considered in the following subsections. In the first, it is assumed that gradient forces saturate, but can be applied independently to each robot. Next, underactuation is also considered.

For both scenarios, the robots are modeled as nonlinear systems with drift, having the same functional form, but different diameters (see Table I) to achieve controllability [10], [5]. Since it was desired to stabilize the robots near the minimum separation distance, controller parameters (Table II) were selected to provide an overdamped response. This enabled the generation of stable trajectories leading from large separation distances to points near the minimum bound that did not involve transients located inside the bound.

TABLE II
Controller Parameters

Parameters	Value
Q-matrix (Diagonal)$\times 10^-4$	$[12, 0, 12, 0, 21, 0, 20, 0]$
R-matrix (Diagonal)$\times 10^-5$	$[1, 1]$
P-matrix	$10 \cdot Q$
dt-Sampling period $[sec]$	0.02
T-Prediction horizon $[sec]$	$50 \cdot 0.02$

A. Minimum Separation Distance Assuming Input Saturation and Independent Robot Control

If it is assumed that there are four independent inputs, ν_i, in (14), instead of two, then each robot can be controlled independently. Using techniques similar to those in [10], it is possible to analytically demonstrate the stability, using NMPC, for all equilibrium points in the open set outside the minimum separation distance bound shown in Fig. 3. Due to length limitations, however, this is beyond the scope of this paper.

As a concise alternative, Figs. 4 and 5 illustrate three robot trajectories converging asymptotically to positions at the minimum distance bound while avoiding collision. The three points lie in the three interaction force regions defined in section II-C. Note that, due to symmetry, these trajectories are representative of all four quadrants. Fig. 4 plots the magnitude of relative distance facilitating comparison with the minimum separation bound. The sum of robot radii, corresponding the collision separation distance, is also shown.

B. Minimum Separation Distance and Trajectories Assuming Input Saturation and Underactuation

Returning to the underactuated system (15) for which the same magnetic gradients are applied to both robots, equilibrium points associated with relative separation distances and angles no longer exist. If, however, the magnetic interaction forces are interpreted as system disturbances then it can be anticipated that the robots can in fact be stabilized in regions *surrounding* a desired relative position.

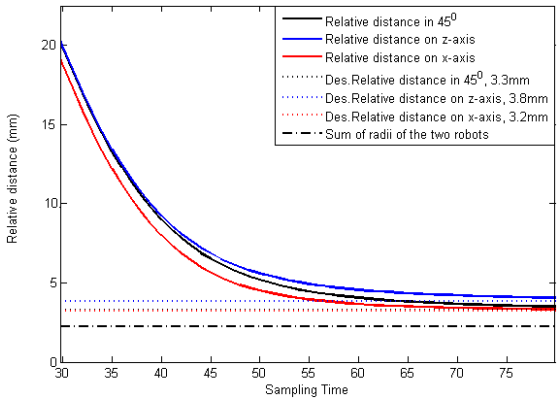

Fig. 4. Separation distance versus time for desired relative angles of $0°$, $45°$, $90°$ and desired relative distances corresponding to the lower bound.

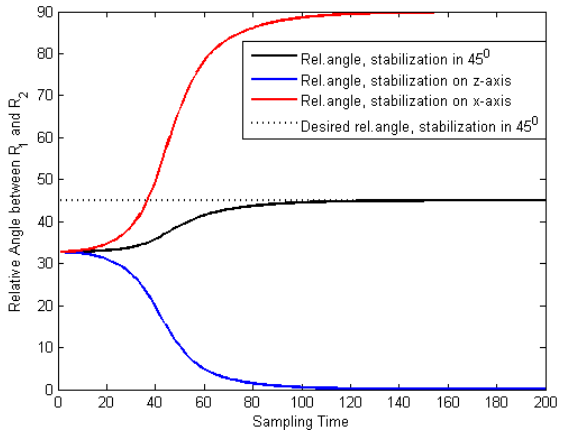

Fig. 5. Relative angle versus time for desired relative angles of $0°$, $45°$, $90°$ and desired relative distances corresponding to the lower bound.

This is illustrated in Figs. 6-8 which show the roughly periodic paths that the robots converge to for three desired relative angles (0,45,90 degrees) located in the three interaction force regions. The open-loop paths, designated by dotted lines are also shown. It is interesting to observe that the distance and angle between the robots closely approach the desired values as shown by the labeled positions in Fig. 6 and as confirmed by the plot of polar coordinates versus time in Figs. 9 and 10. In particular, the distance converges asymptotically to the desired value while the angle oscillates around the desired value.

To understand the effect of underactuation on minimum separation distance, a sequence of simulations were run for relative angles of $\{0, 45, 90\}$degrees. The desired separation distance was initialized at the value of the lower bound derived in section II-D. The distance was then incremented in steps of 0.2mm until the trajectories converged without collision. The resulting minimum distance trajectories are those reported in Figs. 6-10. For comparison with the lower bound of section II-D, these distances are plotted together with the lower bounds in Fig. 3. For this set of robot parameters, the effect of underactuation is to increase the minimum separation distance by a factor of 2.6 on the x and z axes from 3.2 and 3.8mm to 8.5 and 10mm, respectively. In region 2, the distance increases by a factor of 3 from 3.3 to 9.8mm.

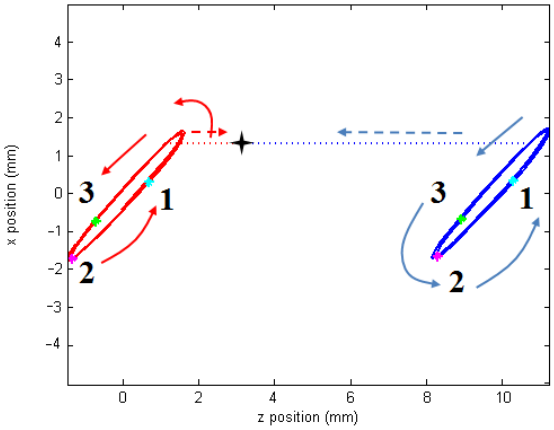

Fig. 6. Closed-loop robot paths for desired relative distance vector, $r = [0, 0, 10]^\top$ mm, i.e., stabilization on the **z**-axis. Corresponding robot locations are numerically labeled. Open-loop paths are also shown resulting in collision at black star.

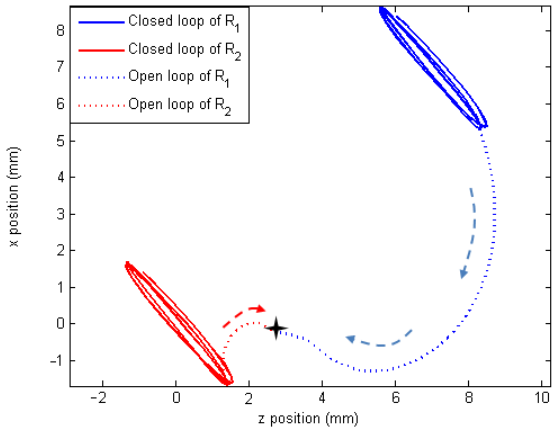

Fig. 7. Closed-loop robot paths for desired relative distance vector, $r = [0, 0, 9.8]^\top$ mm, i.e., stabilization at an angle of $45°$. Open-loop paths are also shown resulting in collision at black star.

V. Conclusions

To enable applications involving multiple magnetic millirobots inside an MRI scanner, it is necessary to be able to navigate them independently. While prior work has addressed independent control under the assumption that the robots are far from each other, this paper is the first to consider the effect of magnetic interaction forces on independent control. This has resulted in several interesting observations.

The first is that, since the magnetic moments of the robots remain aligned with the central field, magnetic interaction torques can be neglected. This results in both attractive and repulsive interaction forces, according to the relative angle between the robots and the central field. A lower bound on separation distance has been derived based on balancing interaction force and saturated magnetic gradient force.

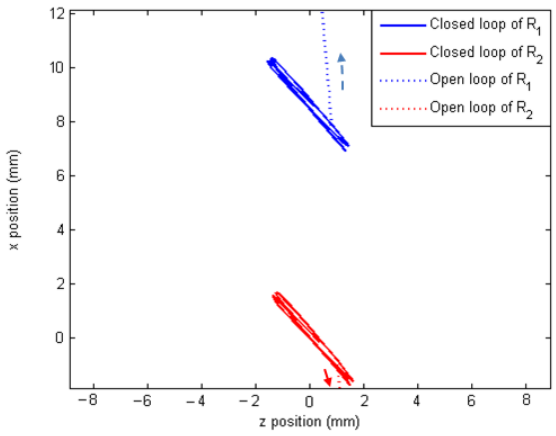

Fig. 8. Closed-loop robot paths for desired relative distance vector, $r = [0, 0, 8.5]^\top$ mm, i.e., stabilization on the **x**-axis. Open-loop paths are also shown resulting in repulsion.

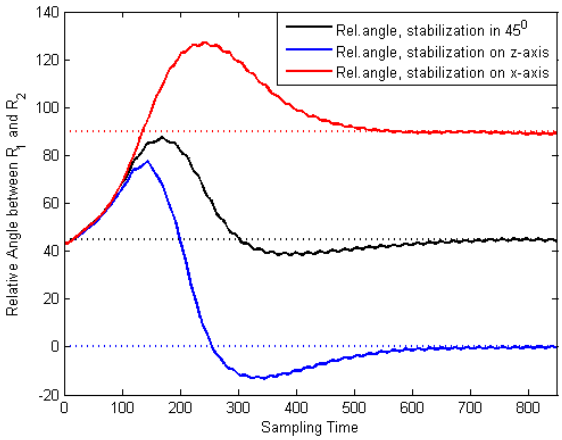

Fig. 10. Relative angle of robots versus time for three cases shown in Fig. 6-8.

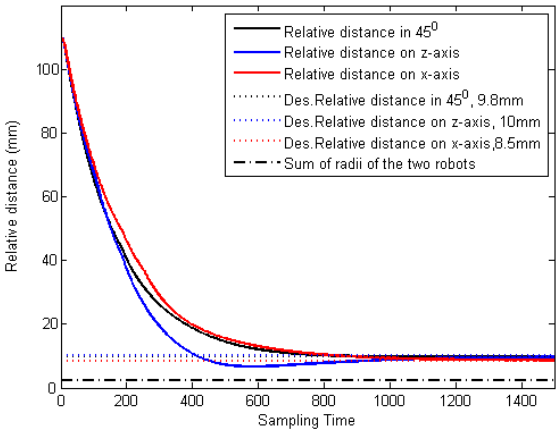

Fig. 9. Relative distance of robots versus time for three cases shown in Figs. 6-8. Collision distance given by sum or robot radii is also plotted.

It has been shown that this bound on separation distance is tight under the assumption of full robot actuation using nonlinear model predictive control. When underactuation is considered, it is demonstrated that this control technique can stabilize robots described by representative parameter values at minimum relative distances 2.5-3 times the lower bound on separation distance.

References

[1] B. Bekham and M. Sitti. Bacterial flagella-based propulsion and on/off motion control of microscale objects. *Ap. Ph. Letters*, 90(2):1–3, 2007.

[2] A.W. Mahoney, N.D. Nelson, K.E. Peyer, B.J. Nelson, and J.J. Abbott. Behavior of rotating magnetic microrobots above the step-out frequency with application to control of multi-microrobot systems. *Applied Physics Letters*, 104(144101):1–4, 2014.

[3] K.B. Yeşin, K. Vollmers, and B.J. Nelson. Modeling and control of untethered biomicrorobots in a fluidic environment using electromagnetic fields. *Int. Journal of Robotics Research*, 25(5-6):527–536, 2006.

[4] M. Hamdi and A. Ferreira. Guidelines for the design of magnetic nanorobots to cross the blood-brain barrier. *Robotics, IEEE Transactions on*, 30(1):81–92, 2014.

[5] P. Vartholomeos, M.R. Akhavan-Sharif, and P.E. Dupont. Motion planning for multiple millimeter-scale magnetic capsules in a fluid environment. *IEEE International Conference on Robotics and Automation (ICRA)*, pages 1927–1932, 2012.

[6] L. Arcese, A. Cherry, M. Fruchard, and A. Ferreira. Dynamic behavior investigation for trajectory control of a microrobot in blood vessels. In *Intelligent Robots and Systems (IROS), 2010 IEEE/RSJ International Conference on*, pages 5774–5779, Oct 2010.

[7] L. Arcese, M. Fruchard, F. Beyeler, A. Ferreira, and B.J. Nelson. Adaptive backstepping and MEMS force sensor for an MRI-guided microrobot in the vasculature. In *Robotics and Automation (ICRA), 2011 IEEE International Conference on*, pages 4121–4126, May 2011.

[8] A.W. Mahoney and J.J. Abbott. Generating rotating magnetic fields with a single permanent magnet for propulsion of untethered magnetic devices in a lumen. *IEEE Transactions on Robotics*, 30(2):411–420, 2014.

[9] E. Diller, S. Floyd, C. Pawashe, and M. Sitti. Control of multiple heterogeneous magnetic microrobots in two dimensions on nonspecialized surfaces. *IEEE Transactions on Robotics*, 28(1):172–182, 2012.

[10] A. Eqtami, O. Felfoul, and P.E. Dupont. MRI-powered closed-loop control for multiple magnetic capsules. *IEEE/RSJ International Conference on Intelligent Robots and Systems*, pages 3536 – 3542, 2014.

[11] E. Diller, J. Giltinan, and M. Sitti. Independent control of multiple magnetic microrobots in three dimensions. *The International Journal of Robotics Research*, 32(5):614–631, 2013.

[12] Aeon Scientific AG. Aeon Phocus, Zürich, Switzerland. http://www.aeon-scientific.com.

[13] C. Bergeles, P. Vartholomeos, L. Qin, and P.E. Dupont. Closed-loop commutation control of an MRI-powered robot actuator. *IEEE International Conference on Robotics and Automation (ICRA)*, pages 698 – 703, 2013.

[14] J.-B. Mathieu and S. Martel. Magnetic microparticle steering within the constraints of an MRI system: proof of concept of a novel targeting approach. *Biomedical Microdevices*, 9:801–808, 2007.

[15] P.B. Landecker, D.D. Villani, and K.W. Yung. An analytic solution for the torque between two magnetic dipoles. In *Magnetic and Electrical Separation*, volume 10, pages 29–33 vol.1, 1999.

[16] P. Vartholomeos, L. Qin, and P.E. Dupont. MRI-powered actuators for robotic interventions. *Intelligent Robots and Systems (IROS), 2011 IEEE/RSJ International Conference on*, pages 4508–4515, 2011.

[17] K.W. Yung, P.B. Landecker, and D.D. Villani. An analytic solution for the force between two magnetic dipoles. *Magnetic and Electrical Separation*, 9:39–52, 1998.

[18] F. Fontes. A general framework to design stabilizing nonlinear model predictive controllers. *Systems & Control Letters*, 42(2):127–143, 2001.

[19] D. Mayne, J. Rawlings, C. Rao, and P. Scokaert. Constrained model predictive control: Stability and optimality. *Automatica*, 36(6):789–814, 2000.

[20] H. Khalil. *Nonlinear Systems*. Prentice-Hall, 2002.